

# **Supplementary material of “A new process-based and scale-respecting desert dust emission scheme for global climate models – Part I: description and evaluation against inverse modeling emissions”**

Danny M. Leung<sup>1</sup>, Jasper F. Kok<sup>1</sup>, Longlei Li<sup>2</sup>, Gregory S. Okin<sup>3</sup>, Catherine Prigent<sup>4</sup>, Martina Klose<sup>5</sup>, Carlos Pérez García-Pando<sup>6,7</sup>, Laurent Menut<sup>8</sup>, Natalie M. Mahowald<sup>2</sup>, David M. Lawrence<sup>9</sup>, and Marcelo Chamecki<sup>1</sup>

<sup>1</sup>Department of Atmospheric and Oceanic Sciences, University of California – Los Angeles, Los Angeles, California, USA

<sup>2</sup>Department of Earth and Atmospheric Sciences, Cornell University, Ithaca, New York, USA

<sup>3</sup>Department of Geography, University of California – Los Angeles, Los Angeles, California, USA

<sup>4</sup>Sorbonne Université, Observatoire de Paris, Université PSL, CNRS, LERMA, Paris, France

<sup>5</sup>Institute of Meteorology and Climate Research (IMK-TRO), Department Troposphere Research, Karlsruhe Institute of Technology (KIT), Karlsruhe, Germany

<sup>6</sup>Barcelona Supercomputing Center (BSC), Barcelona, Spain

<sup>7</sup>Catalan Institution for Research and Advanced Studies (ICREA), Barcelona, Spain

<sup>8</sup>Laboratoire de Météorologie Dynamique, École Polytechnique, Institut Polytechnique de Paris, Ecole Normale Supérieure, Sorbonne Université, CNRS, Palaiseau, France

<sup>9</sup>Climate and Global Dynamics Laboratory, National Center for Atmospheric Research, Boulder, Colorado, USA

*Correspondence to:* Danny M. Leung (dannymleung@ucla.edu)

## Sect. S1. Converting the volumetric soil moisture to the gravimetric soil moisture.

The conversion from volumetric to gravimetric soil moisture is documented in many papers, such as in Oleson et al. (2013). We followed Kok et al. (2014b) and adopted a globally constant soil particle density of  $\rho_p = 2650 \text{ kg m}^{-3}$ . Then we used the MERRA-2 global soil porosity (poros,  $\varphi$ , Fig. S1b) to yield the bulk density of soil  $\rho_b$ :

$$\rho_b = \rho_p(1 - \varphi) \quad (\text{S1})$$

Then, using the water density of  $\rho_w = 1000 \text{ kg m}^{-3}$ , we converted the MERRA-2 volumetric soil moisture (SFMC,  $\theta$ ,  $\text{m}^3 \text{ water} / \text{m}^3 \text{ soil}$ , Fig. S1a) to gravimetric moisture  $w$  (kg water / kg soil, Fig. S1c):

$$w = \frac{\rho_w}{\rho_b} \theta \quad (\text{S2})$$

## Section S2. Description of the Comola et al. (2019) intermittency scheme coupled with Kok et al. (2014b) dust emission equation

In the C19 scheme, the dust emission flux  $F_d$  is calculated using the impact threshold ( $u_{*it}$ ) instead of either the fluid ( $u_{*ft}$ ) or a combined threshold ( $u_{*t}$ ). Following the reasoning in Comola et al. (2019b), we update K14 (Eq. 7) with  $u_{*it}$  instead of  $u_{*t}$  as the threshold (see Sect. 2 for the description of K14 and dust emission thresholds):

$$F_d = C_{tune} C_d f_{bare} f_{clay} \frac{\rho_a(u_{*s}^2 - u_{*it}^2)}{u_{*it}} \left( \frac{u_{*s}}{u_{*it}} \right)^{\frac{C_\alpha(u_{*st} - u_{*st0})}{u_{*st0}}} \quad \text{for } u_* > u_{*it} \quad (\text{S3a})$$

where  $u_{*st} = u_{*ft} \sqrt{\rho_a / \rho_{a0}}$  is the same standardized fluid threshold as in the default K14 scheme. Because  $u_{*it} < u_{*ft}$ , this modified equation accounts for more small dust fluxes that occur due to turbulent winds intermittently driving transport even when  $u_* < u_{*ft}$ . These fluxes are important over marginal source regions for which emissions are otherwise missed by employing  $u_{*ft}$  as the threshold (Comola et al., 2019b).

Next, we account for the intermittency effect on dust emissions by following C19 in introducing the intermittency factor  $\eta$ , which denotes the fraction of time that saltation is active in a model time step (e.g.,  $\sim 30$  mins).  $\eta$  corrects the horizontal sand saltation flux, but since dust emission flux scales with saltation flux (Shao et al., 1993),  $\eta$  is also the fraction of time that dust emission is active in a model timestep. We thus account for the effect of intermittency by multiplying the dust emission flux by  $\eta$  (Comola et al., 2019):

$$F_{d,\eta} = \eta F_d \quad (\text{S3b})$$

where  $\eta \in [0,1]$ .

C19 determines  $\eta$  using the average wind speed, wind fluctuations, and the saltation (and thus dust emission) thresholds. C19 parameterizes  $\eta$  using information at the typical saltation height of  $z_{sal} = 0.1 \text{ m}$ , so we need to first define  $u_{ft}$ ,  $u_{it}$ , and  $u_s$  to be  $u_{*ft}$ ,  $u_{*it}$ , and  $u_{*s}$  translated to the height of  $z_{sal}$  using the log law of the wall:

$$u_X(z_{sal}) = \frac{u_{*X}}{k} \ln \left( \frac{z_{sal}}{z_{0a}} \right) \quad (\text{S4a})$$

where subscript  $X$  could be  $ft$ ,  $it$  or  $s$ ,  $u(z_{sal})$  is the wind speed at saltation height  $z_{sal}$ ,  $z_{0a}$  is the aeolian roughness length taken here as  $10^{-4} \text{ m}$  for simplicity (see Martin and Kok, 2018), and  $k =$

0.386 is the von Kármán constant in the atmospheric boundary layer (Andreas et al., 2006). To parameterize the effect of turbulent wind fluctuations on saltation intermittency, we further define  $\tilde{u}$  to be the instantaneous wind speed at  $z_{\text{sal}}$ , which is described by a normal distribution with a mean equal to the model time step mean  $u$  and a standard deviation  $\sigma_{\tilde{u}_s}$  (Chu et al., 1996), and  $u_s$  and  $\sigma_{\tilde{u}_s}$  are defined for a time interval of  $> 10$  min. Comola et al. (2019) then showed that the  $\sigma_{\tilde{u}}$  parameterization using Monin-Obukhov similarity theory (MOST) worked well for in-situ measurements of horizontal saltation fluxes.  $\sigma_{\tilde{u}}$  is height invariant and can be parameterized using MOST as (Panofsky et al., 1977):

$$\sigma_{\tilde{u}_s} = u_{*s} \left( 12 - 0.5 \frac{z_i}{L} \right)^{1/3} \quad \text{for } 12 - 0.5 \frac{z_i}{L} \geq 0 \quad (\text{S4b})$$

where  $L$  is the Monin-Obukhov length and  $z_i$  is the planetary boundary layer (PBL) height. In boundary-layer meteorology, turbulence is generated by mechanical shear and buoyancy (Stull, 1988). The shear-driven turbulence in a flow scales with  $u_{*s}$ , while the buoyancy-driven turbulence scales with  $z_i/L$ . According to Eq. (20b), high-frequency wind fluctuations ( $\sigma_{\tilde{u}_s}$ ) increase with shear ( $u_{*s} > 0$ ) and buoyancy ( $L < 0$ ). For larger wind fluctuations  $\sigma_{\tilde{u}_s}$ , it is easier for  $\tilde{u}_s$  to sweep across  $u_{it}$  and shut off dust emission, leading to  $\eta < 1$ . As a result, the emission flux predicted by our scheme will be smaller than the other existing parameterizations for  $u_s > u_{ft}$ . If  $u_s \gg u_{ft}$ ,  $\tilde{u}_s$  will be less likely to sweep across  $u_{it}$  and  $\eta$  will approach 1. Furthermore, when  $u_{it} < u_s < u_{ft}$ ,  $\eta$  will be much smaller than one and closer to zero, leading to a small emission flux when other parameterizations predict a zero emission flux. When  $u_s < u_{it}$ ,  $\eta$  could also be greater than zero when  $\sigma_{\tilde{u}_s}$  is large enough so that the instantaneous  $\tilde{u}_s$  crosses through  $u_{it}$ , but the DPM employed would not generate any emission anyway according to Eq. S3a.

With saltation-height variables defined, the total fraction of time  $\eta$  when saltation is active in a model timestep is then formulated as:

$$\eta = 1 - P_{ft} + \alpha(P_{ft} - P_{it}) \quad (\text{S5})$$

where  $P_{it} = P(\tilde{u}_s < u_{it})$  is the cumulative probability that the instantaneous wind  $\tilde{u}$  does not exceed the impact threshold  $u_{it}$ , and  $P_{ft} = P(\tilde{u}_s < u_{ft})$  is the cumulative probability that  $\tilde{u}_s$  does not exceed the fluid threshold  $u_{ft}$ . The fluid threshold crossing fraction  $\alpha$  is defined as the fluid threshold crossing rate  $C_{ft}$ , which is the number of times  $\tilde{u}_s$  sweeps across  $u_{ft}$  per second, divided by the total crossing rate  $C_{ft} + C_{it}$ , which is the number of times  $\tilde{u}_s$  sweeps across  $u_{ft}$  and  $u_{it}$  per second:  $\alpha = \frac{C_{ft}}{C_{ft} + C_{it}}$ .  $\alpha$  approaches 1 when instantaneous wind  $\tilde{u}_s$  mostly crosses  $u_{ft}$ , and approaches 0 when  $\tilde{u}$  mostly crosses  $u_{it}$ . C19 showed that  $\alpha$  is a function of  $u_s$ ,  $\sigma_{\tilde{u}}$ ,  $u_{it}$ , and  $u_{ft}$ :

$$\alpha \approx \left[ \exp\left(\frac{u_{ft}^2 - u_{it}^2 - 2u_s(u_{ft} - u_{it})}{2\sigma_{\tilde{u}_s}^2}\right) + 1 \right]^{-1} \quad (\text{S6a})$$

such that  $\alpha \rightarrow 1$  in the limit of  $u_s \gg u_{ft}$ , and  $\alpha \rightarrow 0$  for  $u_s \rightarrow 0$  and  $\sigma_{\tilde{u}_s} \rightarrow 0$ . As for  $P_{ft}$  and  $P_{it}$ , assuming a Gaussian distribution for  $\tilde{u}$ , i.e.,  $\tilde{u}_s \sim \mathcal{N}(u_s, \sigma_{\tilde{u}_s}^2)$ ,  $P_{ft}$  and  $P_{it}$  can be expressed using the error functions  $\text{erf}(x)$  as:

$$P_{ft} = \frac{1}{2} \left[ 1 + \text{erf}\left(\frac{u_{ft} - u_s}{\sqrt{2}\sigma_{\tilde{u}_s}}\right) \right] \quad (\text{S6b})$$

$$P_{it} = \frac{1}{2} \left[ 1 + \text{erf}\left(\frac{u_{it} - u_s}{\sqrt{2}\sigma_{\tilde{u}_s}}\right) \right] \quad (\text{S6c})$$

Within a model timestep, dust emission is continuous for the fraction of time  $1 - P_{ft}$  when  $\tilde{u}_s > u_{ft}$ , and for the fraction of time  $P_{ft} - P_{it}$  dust emission is in the hysteresis regime ( $u_{it} <$

$\tilde{u}_s < u_{ft}$ ) where dust emission can only be active for a fraction of time  $\alpha$  when  $\tilde{u}_s$  crossed  $u_{ft}$  more recently than  $u_{it}$  in the hysteresis regime. Using Eqs. S3–S6, we computed  $\eta$  from Eq. S3b, yielding the dust emission flux  $F_{d,\eta}$  that accounts for the effects of intermittency.

### Section S3. Calculating the Obukhov length $L$ from MERRA-2 meteorological fields

MERRA-2 does not include the Obukhov length  $L$ , but outputs several variables that allows us to compute  $L$ , using (Golder, 1972; Essa, 2000; Bonan, 2015):

$$L = -\rho_a c_p T u_*^3 / k g H, \quad (\text{S7})$$

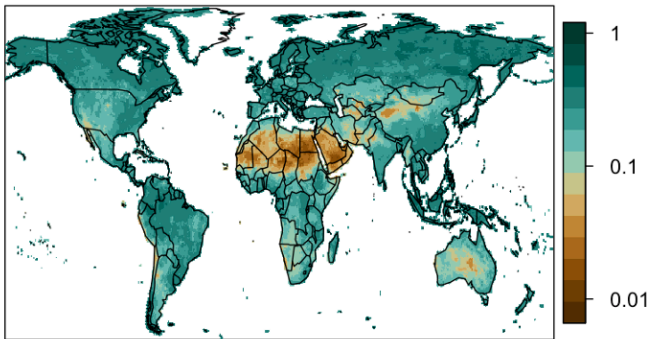
where  $\rho_a$  is air density ( $\text{kg m}^{-3}$ ),  $c_p$  is the specific heat capacity of air under constant pressure ( $\text{J kg}^{-1} \text{K}^{-1}$ ),  $T$  is air temperature (in this study we chose  $T_{10}$ , which is air temperature at the height of 10 m),  $u_*$  is friction velocity ( $\text{m s}^{-1}$ ),  $k$  is the Von Karmen constant,  $g$  is gravitational acceleration ( $\text{m s}^{-2}$ ), and  $H$  is the sensible heat flux ( $\text{W m}^{-2}$ ). MERRA-2 provides sensible heat flux (SHLAND) and  $T_{10}$  (T10M), allowing us to directly compute  $L$ .

Table S1. Past studies employed in this paper that collected dry soil aggregate size distributions over different countries.

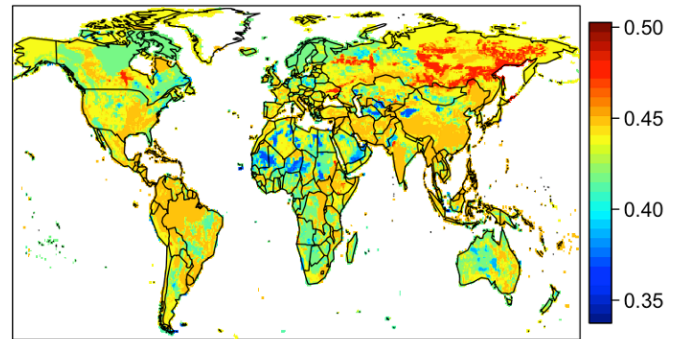
Study	Number of samples we used	Location of the sites	Aridity <sup>a</sup>
Ciric et al. (2012)	5	Pannonian Basin, Serbia	nonarid
Li et al. (2014)	4	Tarim Basin	arid
Wagner et al. (1992)	2	Kansas	arid
Chandler et al. (2004)	3	Columbia Plateau	arid
Mei et al. (2004)	4	Northern China	arid
Swet and Katra (2016)	2	Negev, Israel	arid
Mirzamostafa et al. (1998)	2	Kansas	nonarid
Liu et al. (1998)	3	Inner Mongolian Plateau & Tengger Desert, China	arid
Kalhor et al. (2017)	6	Loess Plateau	nonarid
Su et al. (2007)	4	Hexi Corridor	arid
Udom and Ogunwole (2015)	4	Port Harcourt, Nigeria	nonarid
Malobane et al. (2019)	2	University of Fort Hare	nonarid
Klose et al. (2017)	5	New Mexico	arid
Shao et al. (2011)	1	Victoria, Australia	arid

<sup>a</sup>The aridity of the sampling site was classified by this study based on whether the annual mean MERRA-2 LAI (see Fig. 3a in the main text) is smaller or larger than 1.

a) Volumetric soil moisture ( $\text{m}^3 \text{ water} / \text{m}^3 \text{ soil}$ )



b) Volumetric soil porosity ( $\text{m}^3 \text{ void} / \text{m}^3 \text{ soil}$ )



c) Gravimetric soil moisture ( $\text{kg water} / \text{kg soil}$ )

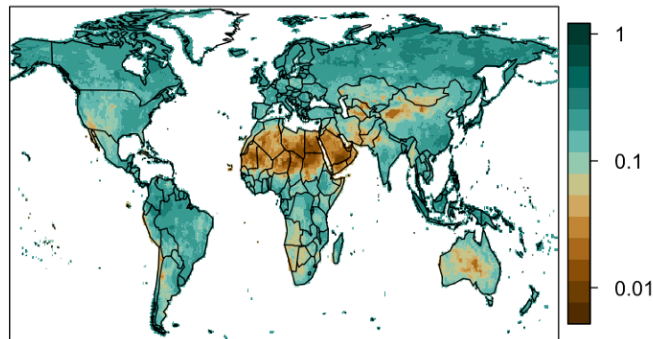


Figure S1. MERRA-2 soil moisture for the year 2006 used in this study. (a) Volumetric soil moisture ( $\text{m}^3 \text{ m}^{-3}$ ), (b) soil porosity, and (c) gravimetric soil moisture ( $\text{kg kg}^{-1}$ ).

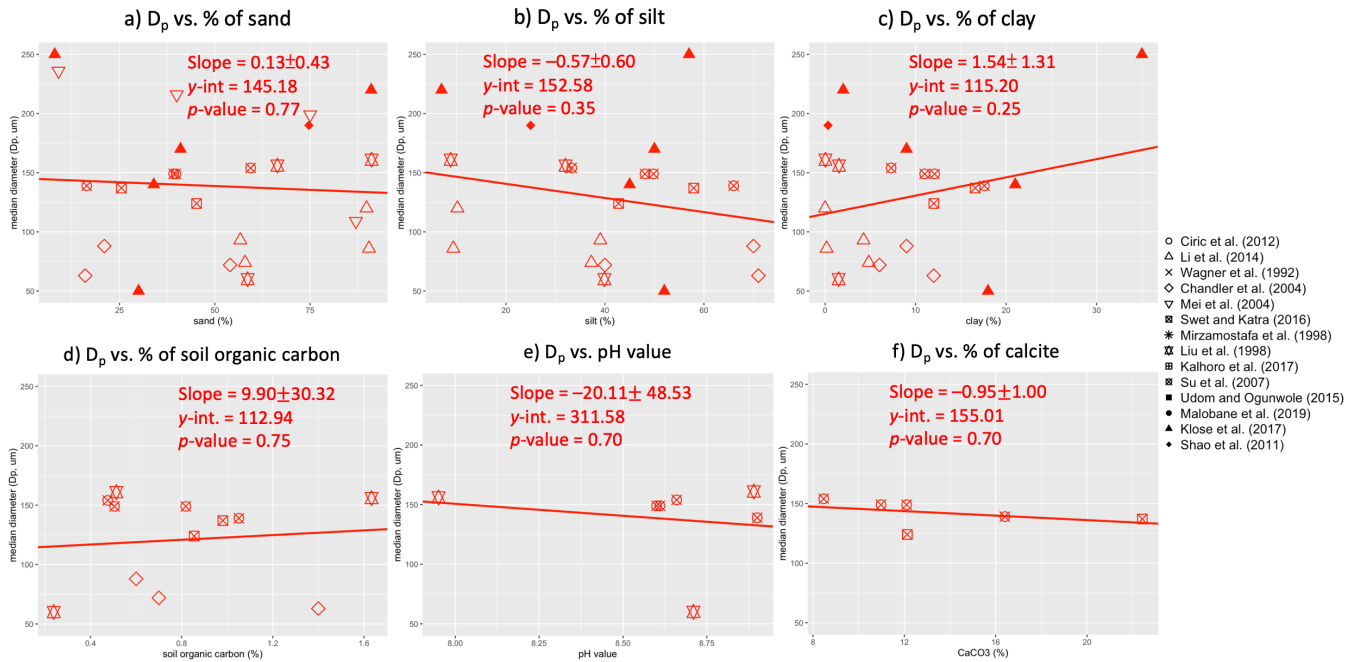


Figure S2. The relationships between soil median diameter  $\bar{D}_p$  and soil texture and other soil properties documented in multiple past studies for arid regions. We relate  $D_p$  to content of (a) sand, (b) silt, (c) clay in %, as well as to (d) soil organic carbon (SOC) content in %, (e) pH value, and (f) % of calcite ( $\text{CaCO}_3$ ). The symbols show the name of each individual study and lines denote linear regressions for which statistics are included for each panel. Studies may not have documented certain texture or properties, so some plots have fewer data points (especially for soil properties).

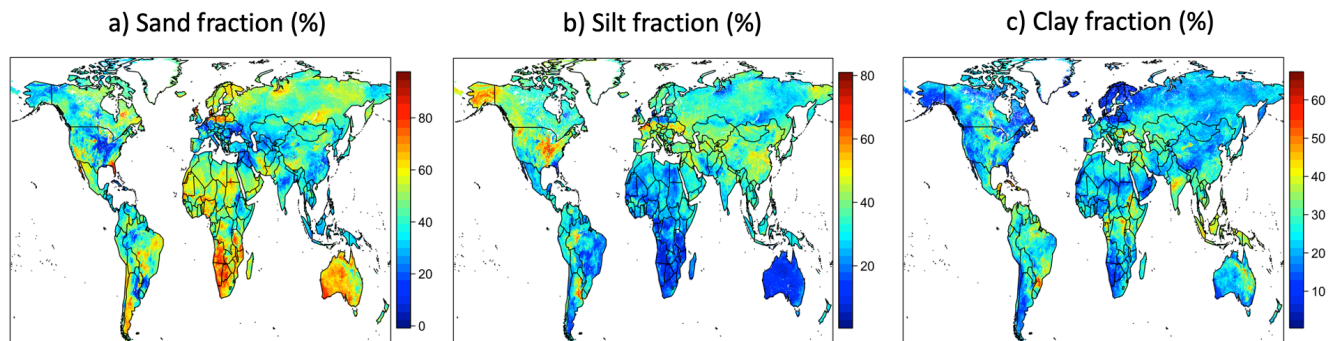


Figure S3. The SoilGrids global  $0.1^\circ \times 0.1^\circ$  maps of (a) sand, (b) silt, and (c) clay in % (Hengl et al., 2017).

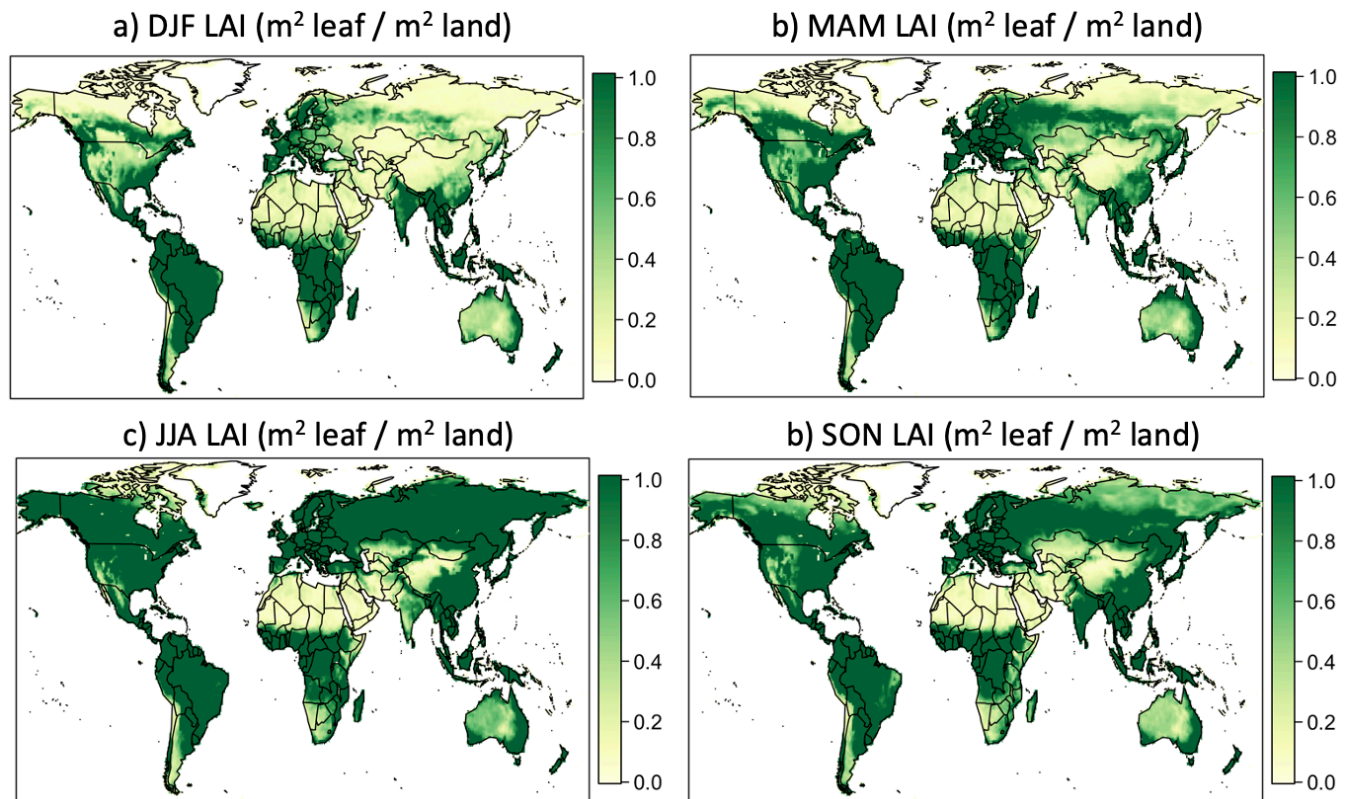


Figure S4. Global distributions of MERRA-2 seasonal mean LAI for the year 2006. Four seasonal mean LAI maps are plotted, including the (a) December–January–February, (b) March–April–May, (c) June–July–August, and (d) September–October–November. The color bar saturates at 1, so regions in dark green color have LAI > 1 and are defined as non-arid area in this study.

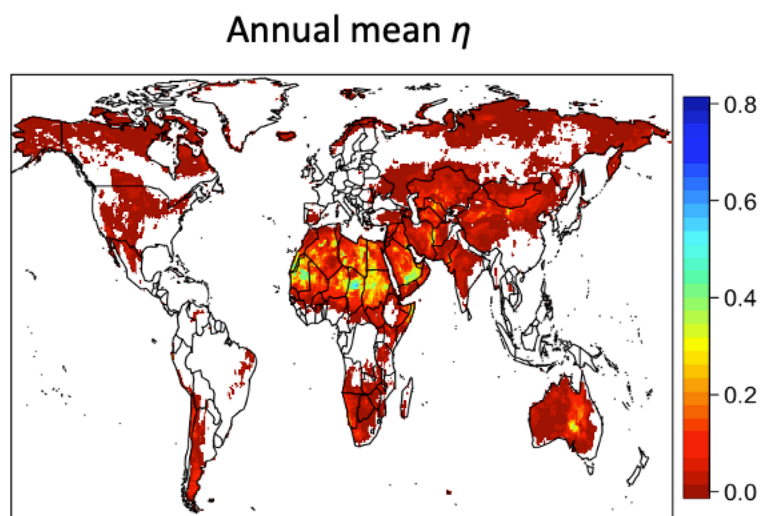


Figure S5. The annual mean intermittency factor  $\eta$ , which denotes the fraction of time within a time step that emission is active, averaged over the whole year 2006.

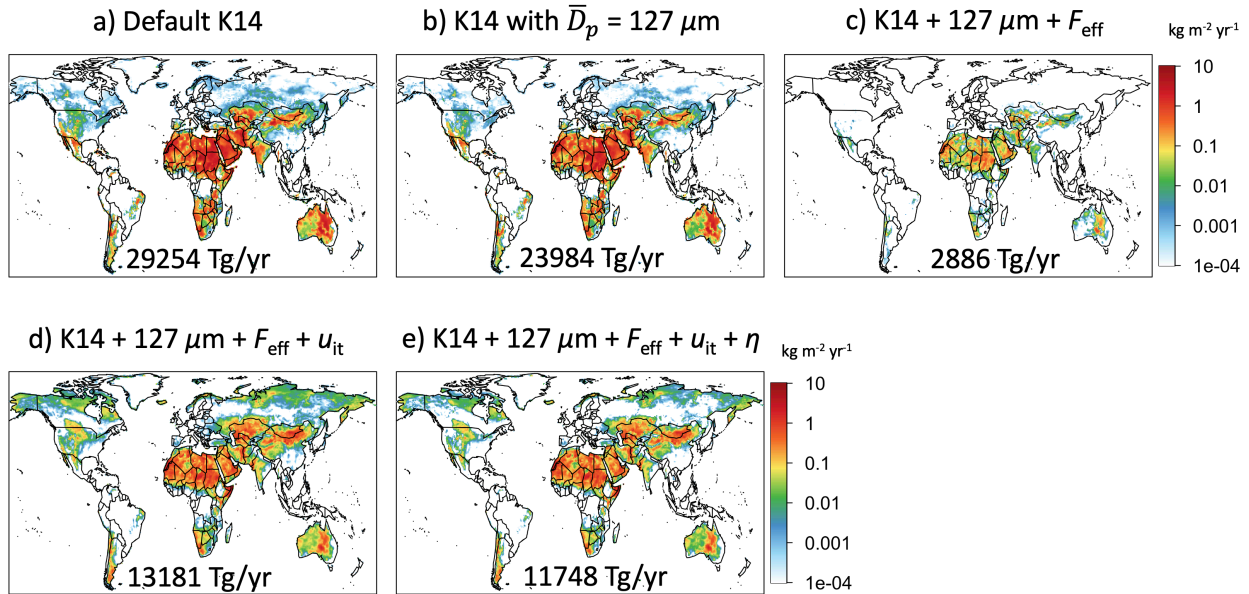


Figure S6. Spatial patterns of the dust emission flux for each modification of the default dust emission scheme. The plots include results for the (a) default K14 scheme (expt. I), (b) K14 with changed soil particle diameter only (expt. II), (c) K14 with the new soil particle diameter and drag partition effect (expt. III), (d) K14 with the new soil particle diameter, drag partition effect, and impact threshold (expt. IV), and (e) K14 with all modifications, i.e., our new scheme (expt. V). All plots are normalized to have a global total emission of  $5000 \text{ Tg yr}^{-1}$ , while each panel also notes the unnormalized global total emission.

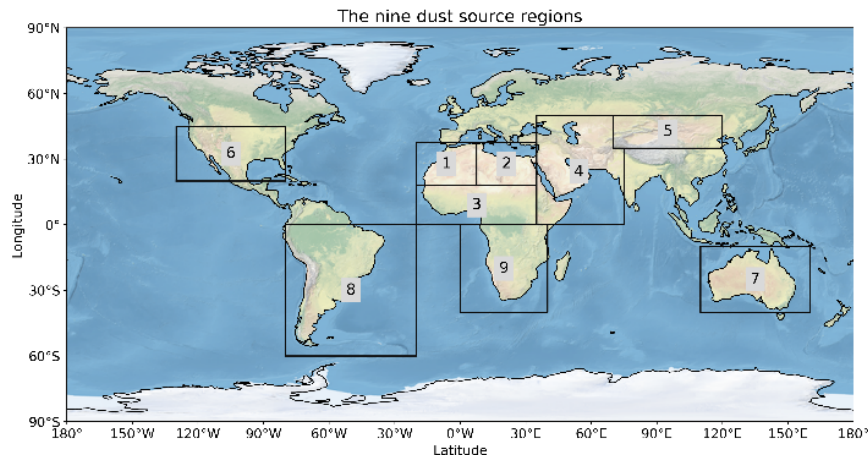


Figure S7. Coordinates of the nine main dust source regions in Kok et al. (2021a) adapted in this study. The coordinates of the nine source regions are: (1) western North Africa (20°W – 7.5°E; 18°N – 37.5°N), (2) eastern North Africa (7.5°E – 35°E; 18°N – 37.5°N), (3) the Sahel (20°W – 35°E; 0°N – 18°N), (4) Middle East / Central Asia (30°E – 70°E for 0°N – 35°N, and 30 – 75°E for 35 – 50°N), (5) East Asia (70°E – 120°E; 35°N – 50°N), (6) North America (130°W – 80°W; 20°N – 45°N), (7) Australia (110°E – 160°E; 10°S – 40°S), (8) South America (80°W – 20°W; 0°S – 60°S), and (9) Southern Africa (0°E – 40°E; 0°S – 40°S). The graph is adopted from Kok et al. (2021a).

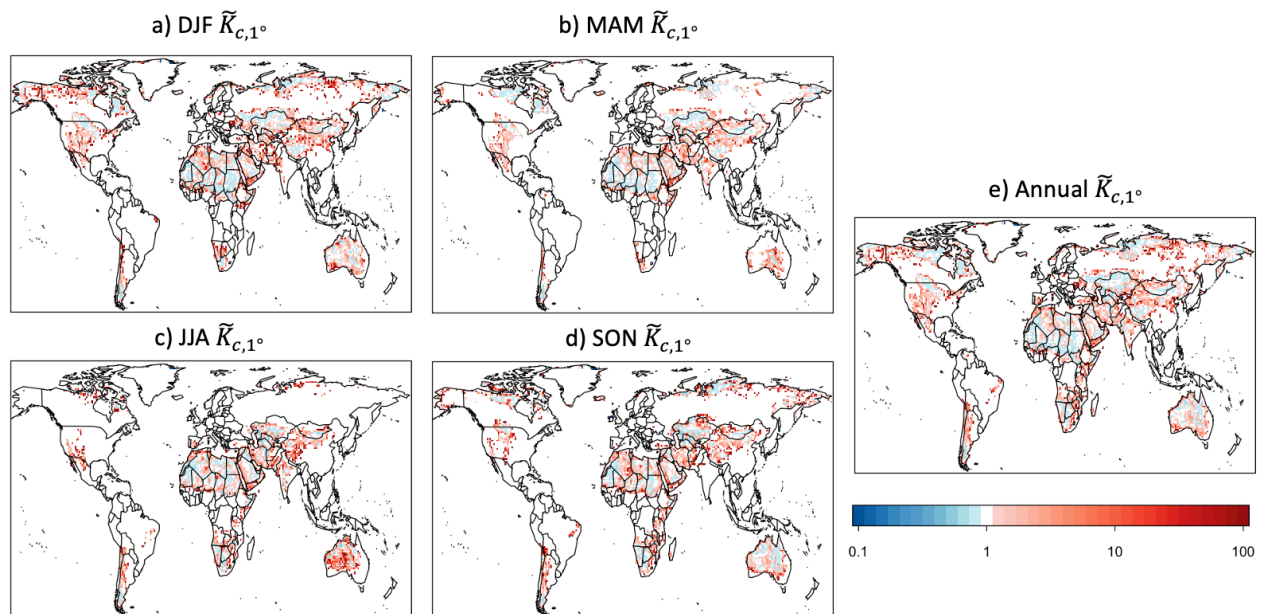


Figure S8. Seasonal variability in the correction map  $\tilde{K}_c$  at a resolution of  $0.9^\circ \times 1.25^\circ$ , for (a) December–January–February, (b) March–April–May, (c) June–July–August, (d) September–October–November, and (e) the whole year.

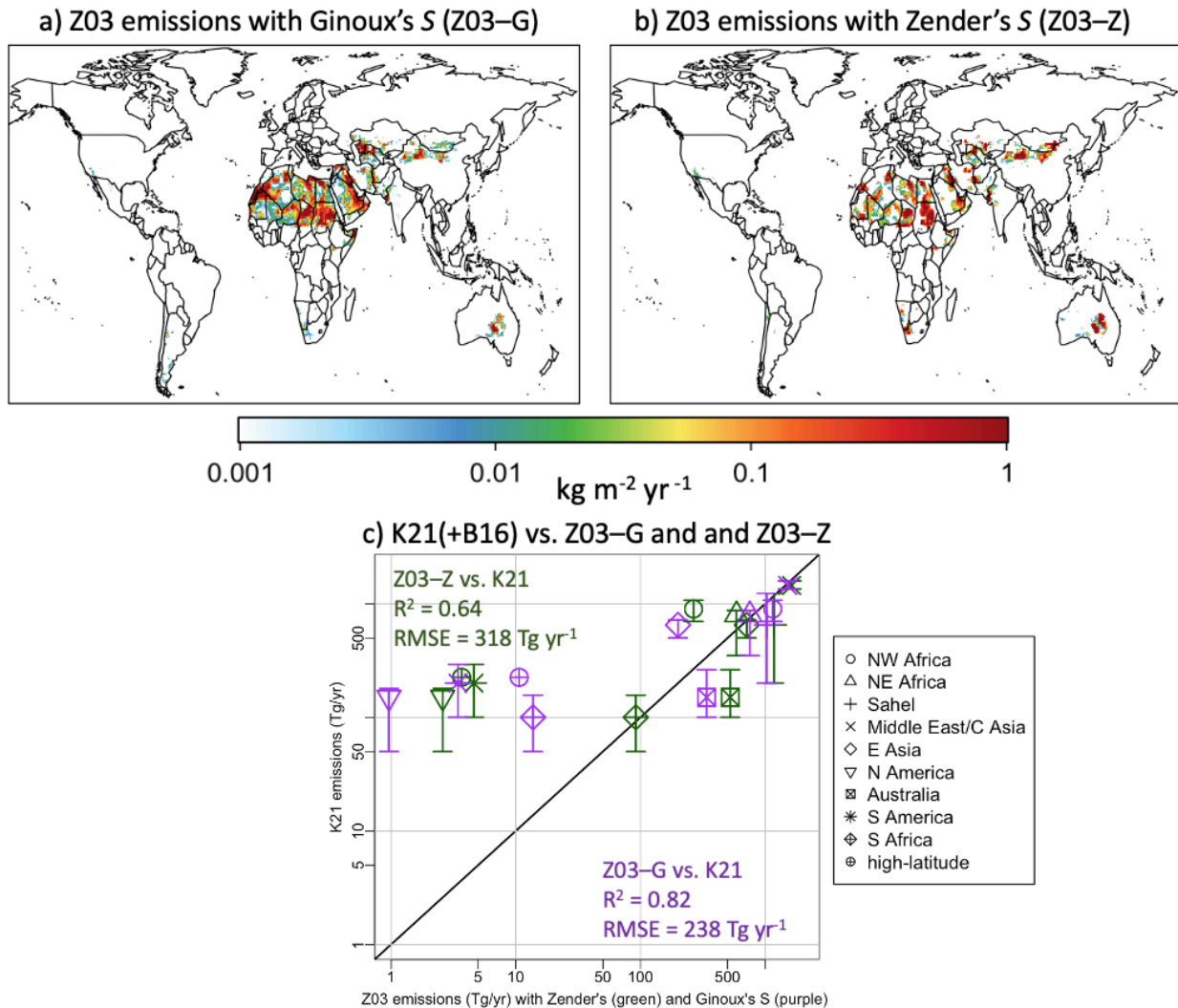


Figure S9. Kok et al. (2021a, b) DustCOMM emissions versus the dust emission simulations using the Zender et al. (2003a) scheme with different source functions  $S$ . (a) Globally gridded Zender et al. (2003a) emissions ( $\text{kg m}^{-2} \text{ yr}^{-1}$ ) with source function  $S$  from Ginoux et al. (2001) (Z03-G). (b) Globally gridded Zender et al. (2003a) emissions ( $\text{kg m}^{-2} \text{ yr}^{-1}$ ) with source function  $S$  from Zender et al. (2003b) (Z03-Z). Both (a) and (b) panels are normalized to 5000 Tg yr<sup>-1</sup> annual global total emissions. (c) Kok et al. (2021a, b) DustCOMM regional emissions (obtained from the fifth column of Table 1 in K21b scaled to a global total of 5000 Tg yr<sup>-1</sup>) versus the regional emissions computed by the Z03-G scheme and the Z03-Z scheme. The regional emissions are obtained following the nine source regions in Fig. 10a, with one extra point being the “high-latitude” emissions obtained from the Bullard et al. (2016) estimation. The error bars show one standard error, except that the B16 high-latitude emission does not contain any error estimate. The black line shows the 1:1 line.

Soil median diameter used in Menut et al. (2013)

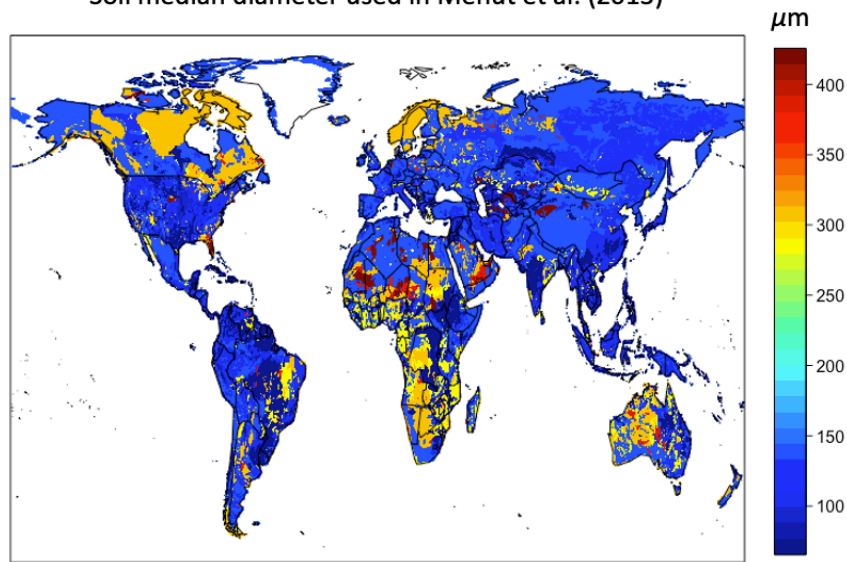


Figure S10. Soil median diameter  $\bar{D}_p$  used in Menut et al. (2013) as an input of the CHIMERE chemical transport model, for the dust emission threshold and drag partition effect calculations.

2006 annual mean MERRA-2 friction velocity (m/s)

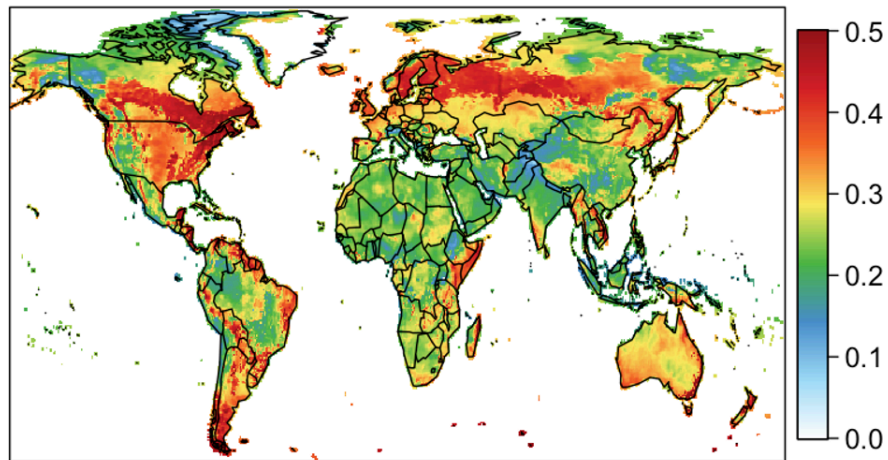


Figure S11. Global distributions of MERRA-2 friction velocity  $u_*$  for the year 2006.

